Research Paper

Impact of a thermoelectric subcooler heat exchanger on a carbon dioxide transcritical refrigeration facility

Álvaro Casi, Patricia Aranguren, Miguel Araiz *, Patricia Alegría, David Astrain

Department of Engineering, Institute of Smart Cities, Public University of Navarre, Campus de Arrosadia s/n E-31006, Pamplona, Spain

ARTICLE INFO

ABSTRACT

To improve the performance of vapour compression refrigeration cycles, the inclusion of a thermoelectric subcooler for low-medium power units has been the focus of recent studies due to its robustness, compactness and simplicity of operation. In thermoelectric systems, it has been demonstrated that the heat exchangers used in the hot and cold side of the thermoelectric modules have a critical impact in the performance of the system. This influence has not yet been studied for thermoelectric subcooling systems in vapour compression cycles. This work, for the first time, evaluates the impact that the heat exchangers of a thermoelectric subcooler, included in a transcritical carbon dioxide refrigeration cycle, have, in the performance of the refrigeration cycle. The influence is quantified in terms of: optimum working conditions, coefficient of performance and cooling capacity. The results show that, through an optimization of the heat exchangers of the thermoelectric subcooler, the performance improvements on the coefficient of performance using this technology are boosted from 11.96 to 14.75 % and the upgrade in the cooling capacity of the system rises from 21.4 to 26.3 %. Moreover, the optimum gas-cooler working pressure of the system is reduced and the optimum voltage supplied to the thermoelectric modules increases.

1. Introduction

The year 2021 reported an increase in electricity demand of 6% and total CO_2 emissions from electric consumption rose by almost 7% according to the International Energy Agency [1,2]. The refrigeration sector in combination with air conditioning and ventilation accounts for 20% of the electricity consumed worldwide and the energy consumption of the sector is expected to double by 2050 [3]. These data highlights the relevance of the refrigeration sector and the paramount importance of energy efficiency in refrigeration facilities to meet decarbonization of the global energy system.

In order to improve the efficiency of vapour compression cycles, many different technologies and configurations have been studied such as: mechanical subcoolers [4], internal heat exchangers [5], parallel compressors [6], multi-stage compression arrangements [7], ejectors [8], expanders [9], thermoelectric subcoolers [10] or a combination of these technologies [11].

For low-medium power units such as vending machines, bottle coolers and display cabinets, most of the technologies studied to improve the efficiency of vapour compression cycles present high economical costs or complex control systems that are not suited for this power range. This emphasizes the need for an easy to control, scalable and low cost solution to improve low-medium refrigeration power units.

Recently, the use of a thermoelectric subcooler has been the focus of many studies to improve the performance of vapour compression cycles and this subcooling technology presents itself as a viable solution for improving the efficiency of low-medium power units.

In a vapour compression refrigeration cycle, a thermoelectric subcooler system (TESC) subcools the refrigerant at the outlet of the gas-cooler/condenser, increasing the cooling capacity of the cycle and, if properly managed, increasing the COP of the refrigeration system. A thermoelectric subcooler is based on the use of thermoelectric modules (TEMs), these devices take advantage of the Peltier effect to transform electrical power into a heat flux without the need of a working fluid. The main advantages of this technology are its robustness, compactness, lack of working fluid and simplicity of operation.

The several advantages of this technology have motivated recent studies regarding the inclusion of a TESC on vapour compression cycles. This idea was firstly proposed by Radermacher and Yang in 2005 through an innovative patent [12]. Later, Schoenfield et al. obtained a 5% increase in the efficiency in an experimental test bench provided with a thermoelectric subcooler assisted by a thermosyphon using R-22 [13]. Afterwards, many authors theoretically studied, using computational models, the improvements that this technology could

---

Nomenclature

Variables

COP	Coefficient of performance
ΔT	Temperature gradient K
h	Enthalpy kJ/kg
I	Current I
$\dot{m}$	Mass flow rate kg/s
$NUSH$	Non useful superheating K
P	Pressure bar
$\dot{Q}$	Heat flux W
R	Thermal resistance K/W
Sub	Subcooling K
T	Temperature K
USH	Useful superheating K
V	Voltage V
$\dot{W}$	Power consumption W
x	Studied variable

Subscripts and superscripts

0	Evaporator
amb	Ambient
$Base$	Base refrigeration cycle
CFD	CFD data
$CO2$	Carbon dioxide
$Cold$	Cold side
$comp$	Compressor
cu	Copper
DC	DC electrical power supply
exp	Experimental data
fan	Fan of the hot side heat exchanger
gc	Gas-cooler
$H0\ C0$	Starting setup of the subcooler
Hot	Hot side
hot_f	Hot face of the heat exchanger
HX	Heat exchanger
in	Inlet
out	Outlet
TEM	Thermoelectric module
$TESC$	Thermoelectric subcooler

achieve: Sarkar predicted an increase in COP of 25.6% and a reduction of discharge pressure of 15.4% [14], Yazawa et al. predicted an increase on maximum cooling performance of 12–13% for a data centre cooling application [15] and finally, Jamali et al. predicted improvements of up to 19% on the COP when a thermoelectric subcooler is included [16].

In 2020, Sanchez et al. obtained an experimental improvement of the COP of 9.9% and an increase in cooling capacity of 16% in a transcritical CO_2 vapour compression refrigeration plant [17]. Subsequently, Aranguren et al. optimized the voltage supplied to the TEMs and the fans of the thermoelectric subcooler, achieving an experimental improvement of 11.3% on the COP and exhibiting the importance of proper optimization of the thermoelectric subcooler [10].

The relevance of the heat exchangers in thermoelectric applications has been demonstrated in both generation and refrigeration applications. Catalan et al. harvested 54% more energy using a thermosyphon heat exchanger in shallow hot dry rock fields [18] and Astrain et al. demonstrated the effect of the heat exchangers used in a thermoelectric refrigerator and its impact on the efficiency [19]. These studies highlight the importance of proper optimization of the heat exchangers in

thermoelectric applications. In regard with thermoelectric subcoolers for vapour compression cycles, the effect that the heat exchangers have in the performance of the system has not yet been studied and this work aims to analyse this influence.

For the first time, the impact that the heat exchangers have in the performance of a thermoelectric subcooler is studied, regarding the: optimum working conditions, cooling capacity, and COP of the whole system. For that, an already validated advanced computational model is used to test the effect of using different heat exchangers in the subcooler, in both the cold and hot side of the thermoelectric modules. In Section 2, the experimental cooling facility and the thermoelectric subcooler in which this work is based are described. Also in Section 2 the computational model used to simulate the whole system is briefly described. In Section 3 the methodology used to characterize the heat exchangers and how they are introduced in the model is explained. The results and the discussion are presented in Section 4 and lastly, conclusions are drawn in Section 5.

2. System modelling

The refrigeration facility and the thermoelectric subcooler system simulated are described in Section 2.1, the main elements of the refrigeration facility are listed and the starting setup of the thermoelectric subcooler is described. The validated computational model used to model the system with different heat exchangers is briefly explained in Section 2.2.

2.1. Cooling facility

The starting point of this work is an experimental cooling facility that uses carbon dioxide as a refrigerant and operates under transcritical conditions along with a thermoelectric subcooler system. The objective of this work is to quantify the effect that using different heat exchangers on the thermoelectric subcooler will have on the cooling facility and up to which COP would be achievable with optimized heat exchangers. For that, the computational model is used to calculate the behaviour of the cooling facility with different heat exchangers.

The experimental system uses a two-stage expansion process to control the pressure of the gas-cooler and the useful superheating of the evaporator. The main elements of the system are: a brazed-plate evaporator with a surface area of $0.567\,\text{m}^2$, 2 electronic valves, an hermetic compressor with a cubic capacity of $1.1\,\text{cm}^3$, a finned gas-cooler under force convection that presents a transfer area of $0.27\,\text{m}^2$ and the thermoelectric subcooler system [10]. An schematic of the refrigeration facility along the P-h diagram of the cycle is presented in Fig. 1.

The thermoelectric subcooler consists of 4 subcooling blocks connected in series at the outlet of the gas-cooler as it is shown in the schematic of Fig. 2, each subcooling block is composed of 1 cold side heat exchanger (C0), 2 TEMs (M), 2 hot side heat sinks (H0) and 2 fans (F0) to help dissipate the heat flux of the hot side heat sinks. The cold side heat exchanger (C0) consists of a solid copper block of $60 \times 74 \times 10\,\text{mm}^3$ that is provided with an interior drilled path and an internal heat exchange area of $0.0037\,\text{m}^2$. The 2 thermoelectric modules used (M) are bismuth-telluride commercial modules from Marlow Industries, RC-8-01L, each module has a total surface are of $40 \times 40\,\text{mm}^2$ and 127 thermocouples. On the hot side, 2 aluminum finned heat sinks (H0) are used, each one is provided with 25 fins and a transfer area of $0.16\,\text{m}^2$. Lastly, 2 axial fans (F0) of 80 mm of diameter are used, each fan consumes 0.78 W at full power.
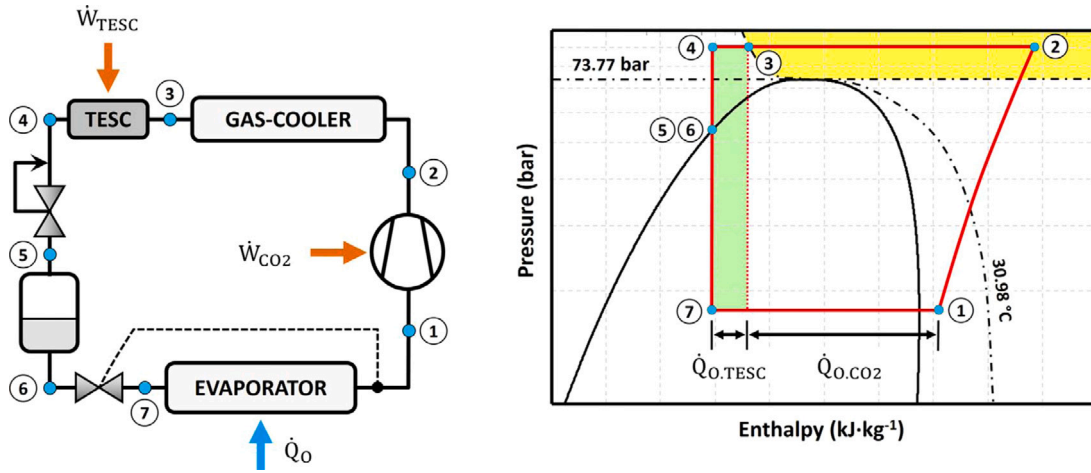
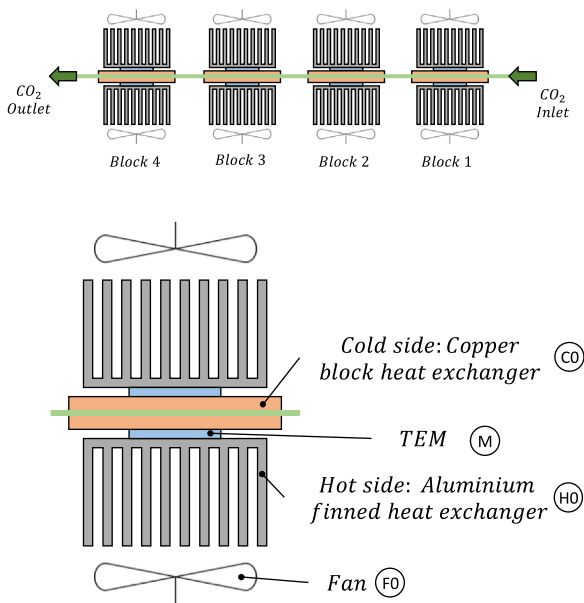**Fig. 1.** Schematic of the refrigeration facility with its P-h diagram [17].

Fig. 2. Schematic of the thermoelectric subcooling system.

Table 1
Inputs for the computational model.

Input	Value
Evaporation temperature (T_0)	−10 °C
Useful superheating (USH)	4 K
Non-useful superheating ($NUSH$)	12 K
Pressure of the gas-cooler (P_{gc})	82–88 bar
Ambient temperature (T_{amb})	30 °C
Voltage supplied to the TEM (V_{TEM})	1–4 V

Table 2
Main outputs of the computational model.

Output	Values
Mass flow rate of the refrigerant ($\dot{m}_{CO2}$)	6.90–7.21 kg h^{-1}
Power consumption of the compressor ($\dot{W}_{comp}$)	272.53–280.06 W
Power consumption of the TESC ($\dot{W}_{TESC}$)	9.53–77.50 W
Cooling power at the evaporator ($\dot{Q}_0$)	315.25–398.67 W
Coefficient of performance (COP)	1.060–1.207

each heat exchanger is introduced in the model as an individual thermal resistance. The model takes into account the 4 thermoelectric effects, temperature dependant thermoelectric properties and the effect of the heat exchangers. Also, the subcooler solves each block of the thermoelectric subcooler separately, increasing the accuracy of the calculation. For that, once the first block is calculated, its outlet is introduced as the starting point for the second subcooling block, this process is repeated for the 4 blocks of the studied thermoelectric subcooler.

The necessary inputs to solve the system are included in Table 1 along their values and units. The model simulates the behaviour of the whole system calculating temperature (T), pressure (P) and enthalpy (h) of each thermodynamic point to obtain the main outputs collected in Table 2.

The behaviour of the subcooler directly depends on the thermal resistance value of the heat exchangers. This highlights the relevance of properly calculating and characterizing the heat exchangers used in the subcooler system. The methodology used to obtain the thermal resistances is described in Section 3. After characterizing the heat exchangers, the computational model is used to calculate the impact of using different heat exchangers in both the hot and cold side of the thermoelectric subcooler, quantifying the impact they have on the efficiency of the whole system.

3. Heat exchanger characterization

The characterization of the heat exchangers and how they are introduced in the computational model is explained in this section.

2.2. Computational model

The vapour compression cycle along the thermoelectric subcooler is simulated using an already published and validated computational model. The model is coded in Matlab and predicts the most important outputs with deviations between the ± 7%.

The vapour compression cycle is simulated under transcritical conditions and Refprop v9.1 is used to obtain the properties and thermodynamic state of points of interest. Useful and non-useful superheating are taking into account. The volumetric and global efficiency of the compressor are introduced as adjusted expressions from previous experimental data. The gas-cooler efficiency is introduced as a function of the gas-cooler pressure and the expansion process at the electronic valves are considered isenthalpic.

The thermoelectric subcooler is simulated using the implicit difference method and the system is discretized homogeneously in 15 unique thermal resistances. The TEM is discretized with 11 resistances to properly predict the thermoelectric effects produced along the TEM. Two thermal resistances correspond to the cold and hot side contact thermal resistance between the heat exchangers and the TEMs. Lastly,

Table 3
Commercial heat sinks tested for the hot side.

	Type	Model
H0	Finned heat sink	Arctic Alpine 64 GT
H1	Pinned heat sink	Alpha PAL8942
H2	Low profile heat pipe	Xigmatek HDT-D982 Durin
H3	High profile heat pipe	Xigmatek HDT-S983 Nepartak

H0   *H1*

H2   *H3*

Fig. 3. Studied heat sinks for the hot side: finned heat sink (H0), pinned heat sink (H1), low profile heat pipe (H2) and heat pipe (H3).

In Section 3.1 the experimental methodology used to study the heat sinks of the hot side of the thermoelectric subcooler is described and Section 3.2 focuses on the computational approach to characterize the heat exchangers of the cold side.

3.1. Hot side heat sinks

For the hot side, 4 different commercial heat sinks with forced convection, including the one used in the experimental setup (H0), are experimentally tested and characterized. The heat sinks allow an easy assemble with the TEMs as they are provided with a planar surface. The 4 heat sinks are listed in Table 3 and can be seen in Fig. 3. The first heat sink, Arctic Alpine 64 GT (H0), is a finned heat exchanger of $84 \times 100 \times 64\,mm^3$, with a total weight of $512\,g$ and is the one assembled in the experimental setup. Alpha PAL8942 (H1), is a pinned heat exchanger of $78 \times 90 \times 63\,mm^3$ and a total weight of $295\,g$. Xigmatek HDT-D982 Durin (H2), is a low profile heat exchanger of $120 \times 92 \times 65\,mm^3$ provided with 2 heat pipe tubes of $8\,mm$ that weights $200\,g$. The last heat sink tested, Xigmatek HDT-D983 Nepartak (H3), is a high profile heat exchanger of $100 \times 62 \times 134\,mm^3$ provided with 3 heat pipe tubes of $8\,mm$ and a total weight of $643\,g$. As the air flow rate produced by the fans in a forced convection heat sink is a really important parameter for their performance [20], each of the heat sinks is experimentally tested and characterized using 4 fans of different air flow rate and power. In addition, each heat sink is tested without the fans to test their performance without auxiliary consumption. Due to their dimensions, H0 and H1 have been tested with 80 mm fans whereas H2 and H3 have been tested with 90 mm fans. The characteristics of the fans used can be seen in Table 4, fans 0 to 3 were used for H0 and H1 whereas fans 4 to 7 were used for H2 and H3.

The heat sinks are tested in a climatic chamber were ambient temperature is set to $30\,°C$ and relative humidity is set to 55%. A heating copper block of $40 \times 40 \times 10\,mm^3$ provided with 6 cartridges heaters is used as a heat source for each heat sink. The voltage supplied to the cartridges is controlled by and adjustable DC electric power supply and a heat flux of 5, 10, 15 and 20 W is forced along each heat sink. Free surfaces of the copper block are insulated with a rockwool layer of $100\,mm$ to ensure that all the heat produced in the cartridges flows through the heat sinks. A temperature probe is located between the copper heating block and the heat sink (T_{hot_f}). Also, 2 temperature probes are situated at the climatic chamber to collect ambient temperature (T_{amb}). The location of the probes and an schematic of the experimental setup are shown in Fig. 4. To calculate the thermal resistance, Eq. (1) is used, temperatures are collected by sensors and the heat flux is obtained trough the electrical power consumption of the DC electrical power supply ($\dot{W}_{DC}$). The power consumption supplied to the cartridges is measured by a DC voltmeter and a DC ammeter. The main characteristics of the sensors used are collected in Table 5

$$R_{HX} = \frac{\Delta T_{HX}}{\dot{Q}_{HX}} = \frac{T_{amb} - T_{hot\_f}}{\dot{W}_{DC}} = \frac{T_{amb} - T_{hot\_f}}{V_{DC} \cdot I_{DC}} \quad (1)$$

Each combination of heat sink and fan is tested for 4 different heat fluxes: 5, 10, 15 and 20 W. As a result, an experimental characterization of each heat sink is obtained as a function of the heat flux, the experimental thermal data is adjusted to a linear function as in Eq. (2)
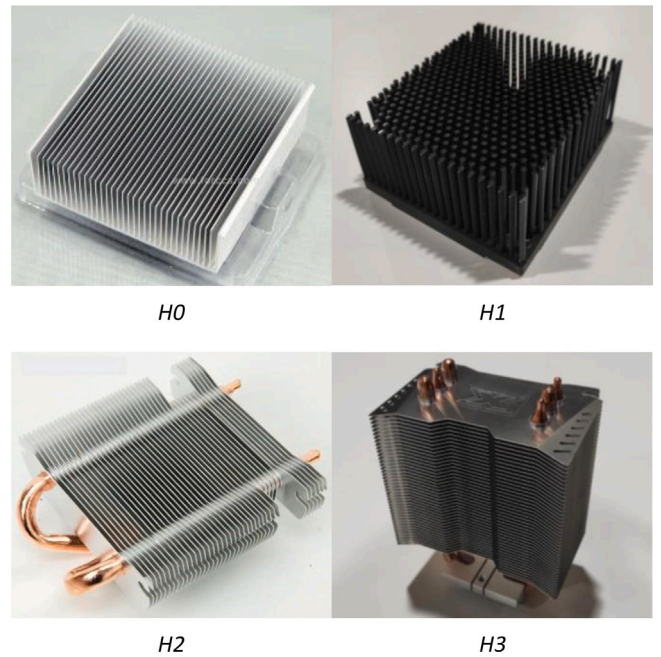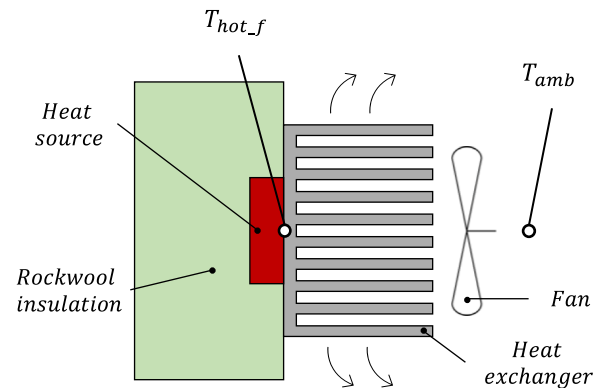

Fig. 4. Schematic of the experimental setup to characterize the hot side heat sinks.

where i corresponds to the heat sink and j to the fan. Some graphic examples of the experimental adjusted linear functions can be seen in Fig. 5. The coefficients for the functions are presented in Tables 6 and 7.

$$R_{Hi\_Fj} = a_{ij} \cdot \dot{Q}_{HX} + b_{ij} \quad (2)$$

The thermal resistance of the heat sinks of the hot side is introduced in the model as a function of the heat flux that passes through them, as in Eq. (2). Using the computational model, the effect of using different heat sinks for the hot side of the thermoelectric subcooler is calculated. The results obtained are presented in Section 4.1.

3.2. Cold side heat exchangers

For the cold side, 2 different heat exchangers are simulated using a Computational Fluid Dynamics (CFD) analysis program, ANSYS Fluent. The heat exchanger used in the experimental setup (C0) alongside an optimized design (C1) are simulated. Heat exchanger C0 consists of a solid copper block of $60 \times 74 \times 10\,mm^3$ with an interior drilled circuit that provides an internal heat exchange area of $0.0037\,m^2$, the cross

Table 4
Main characteristics of the fans used for the thermal characterization.

Hot side heat sink	Fan (Model)	Dimensions mm^3	Air flow (m^3/min)	Static pressure (Pa)	Power consumption (W)
H0 & H1	F0 (MF80251V3-1000U-A99)	80 × 80 × 25	0.93	27	0.78
	F1 (MF80251V2-1000U-A99)	80 × 80 × 25	1.05	37	1.11
	F2 (MF80251V1-1000U-F99)	80 × 80 × 25	1.16	45	1.44
	F3 (EE80251BX-000U-A99)	80 × 80 × 25	1.27	57	1.80
H2 & H3	F4 (MF92251V3-1000U-A99)	90 × 90 × 25	1.12	25	0.90
	F5 (MF92251V2-1000U-A99)	90 × 90 × 25	1.27	32	1.44
	F6 (MF92251V1-1000U-A99)	90 × 90 × 25	1.46	37	1.68
	F7 (PF92251V3-1000U-F99)	90 × 90 × 25	1.84	62	2.97

Table 5
Main characteristics of the sensors for the characterization.

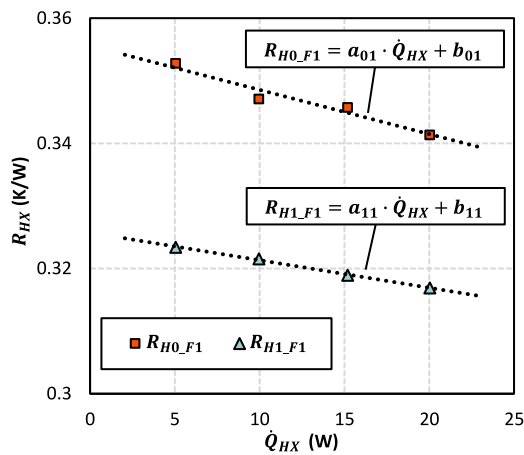| Probe	Measured variable	Accuracy
Thermocouple T	Temperature (°C)	±0.2 °C
Digital voltmeter	DC voltage (V)	±0.5% of reading
Digital ammeter	DC current (A)	±0.2% of reading

Fig. 5. Thermal characterization of H0 and H1 for F1 as a function of the heat flux.

(a) Interior circuit and mesh of the heat exchanger C0

(b) Detail mesh inflation of the fluid for C0

Fig. 6. Interior circuit and mesh of the heat exchanger C0 (a) and detail mesh inflation of the fluid for C0 (b).

section of the path is circular with a diameter of 3 mm. The path of the circuit for C0 can be shown in detail in Fig. 6 alongside the mesh utilized for the simulations. The optimized design, C1, consists of the same solid copper block of $60 \times 74 \times 10\,\text{mm}^3$, the drilled path is divided in two longer levels with a narrower diameter, 1 mm, providing a greater velocity of the fluid at the heat exchanger and increasing the heat transfer area to $0.0044\,\text{m}^2$.

The geometry is imported from a 3D modelling software and a symmetric region is used lengthwise to decrease the computational requirements. Regarding the mesh, an inflation is used in the edges of the fluid circuit to ensure a proper simulation of the boundary layer. An study on the effect of the mesh is performed to verify that the correct amount of elements are used without affecting the final resolution. The final mesh consists of $200\,786$ elements for C0 and $234\,395$ for C1, Fig. 6 shows the mesh used for C0 and a detail of the inflation at the walls of the inner circuit.

The density, specific heat, thermal conductivity and viscosity of the CO_2 are manually introduced as functions depending on temperature and pressure, the properties data are obtained from Refprop v9.1. The density, specific heat and thermal conductivity of the copper are manually introduced as constants. The energy model is activated and viscous model SST k-omega is used. At the inlet of the fluid, a mass flow rate ($\dot{m}_{CO2}$) is introduced from 0.0009 to $0.0011\,\text{kg/s}$ and the inlet temperature of the CO_2 (T_{CO2_in}) is introduced from 16 to 34 °C. At the side of the heat exchanger, in an square area of $40 \times 40\,\text{mm}^2$, where the TEM would be placed, a heat flux ($\dot{Q}_{HX}$) is introduced from 2 to 36 W. These values depend on the working conditions of the
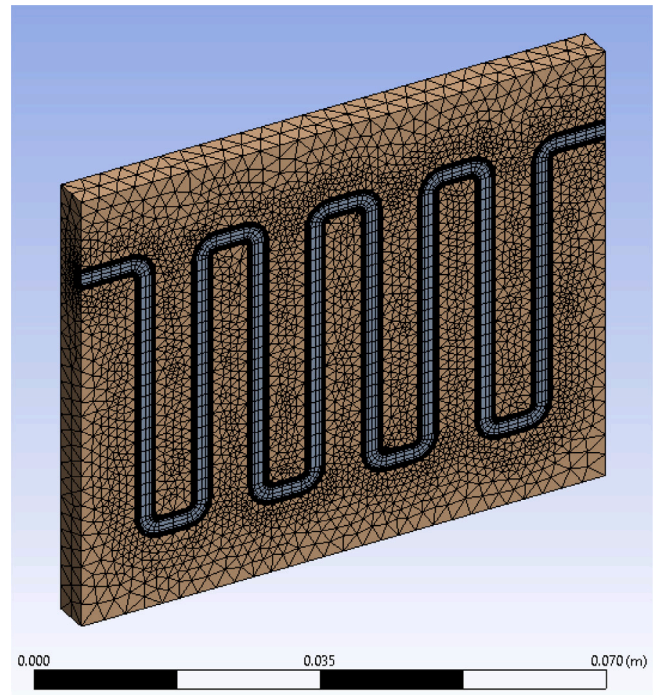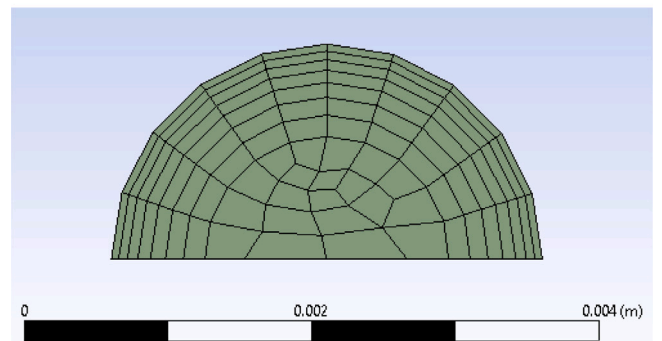
refrigeration cycle and the voltage supplied to the TEM and to precisely characterize the heat exchanger, a wide range of these parameters is simulated. Lastly, the rest of the surfaces are considered adiabatic for the simulations.

The thermal resistance of the heat exchanger is calculated using Eq. (3), where the temperature of the CO_2 (T_{CO2}) is calculated as the average temperature of the fluid in the heat exchanger and the temperature of the copper (T_{cu}) is calculated as the average temperature

Table 6
Coefficients for the adjusted linear functions of the thermal resistance for H0 and H1.

	No Fan	F0	F1	F2	F3
H0	$a_0 = -0.0950156492$	$a_{00} = -0.0004703507$	$a_{01} = -0.0007063978$	$a_{02} = -0.0010353239$	$a_{03} = -0.0011297395$
	$b_0 = +4.9050328451$	$b_{00} = +0.3684773422$	$b_{01} = +0.3556137149$	$b_{02} = +0.3563768312$	$b_{03} = +0.3272372158$
H1	$a_1 = -0.0588765718$	$a_{10} = -0.0000841031$	$a_{11} = -0.0004399484$	$a_{12} = -0.0003650729$	$a_{13} = -0.0004496741$
	$b_1 = +3.2256481545$	$b_{10} = +0.3319042526$	$b_{11} = +0.3257287538$	$b_{12} = +0.3184789105$	$b_{13} = +0.2797354520$

Table 7
Coefficients for the adjusted linear functions of the thermal resistance for H2 and H3.

	No Fan	F4	F5	F6	F7
H2	$a_2 = -0.0926334334$	$a_{24} = -0.0000448850$	$a_{25} = -0.0000182814$	$a_{26} = -0.0002875021$	$a_{27} = -0.0003024696$
	$b_2 = +4.2375064821$	$b_{24} = +0.2730943134$	$b_{25} = +0.2460683247$	$b_{26} = +0.2526199069$	$b_{27} = +0.2257131360$
H3	$c_0 = -0.0501675284$	$a_{34} = -0.0005931052$	$a_{35} = -0.0012341905$	$a_{36} = -0.0012153259$	$a_{37} = -0.0012791407$
	$c_2 = +1.8325094524$	$b_{34} = +0.1957495067$	$b_{35} = +0.21197254875$	$b_{36} = +0.2017640625$	$b_{37} = +0.1817637992$

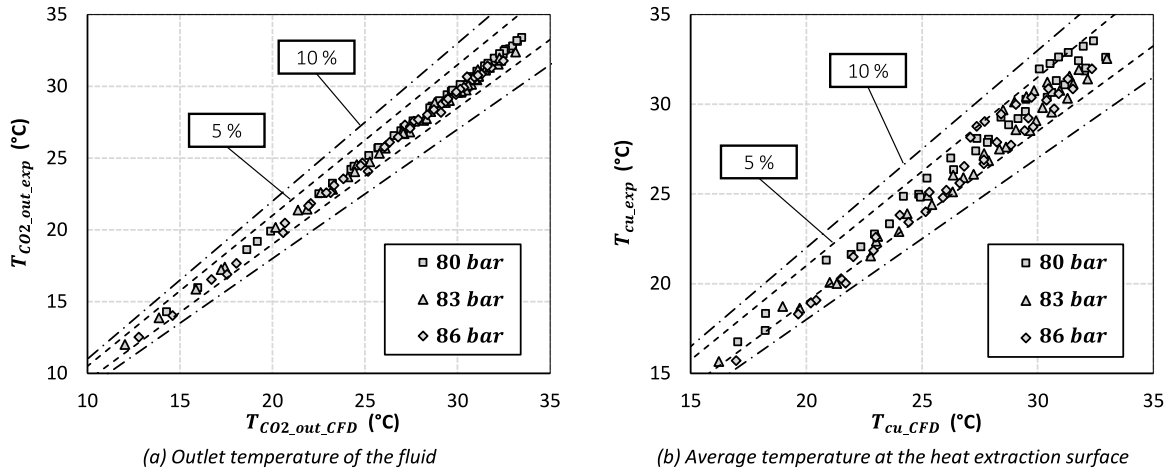(a) Outlet temperature of the fluid   (b) Average temperature at the heat extraction surface

Fig. 7. Comparative between experimental data and CFD data for heat exchanger C0 at 80, 83 and 86 bar for: outlet temperature of the fluid (a) and average temperature at the heat extraction surface (b).

in the square area of $40 \times 40\,mm^2$ where the heat is extracted.

$$R_{HX} = \frac{\Delta T_{HX}}{\dot{Q}_{HX}} = \frac{T_{CO2} - T_{cu}}{\dot{Q}_{HX}} \qquad (3)$$

To prove the veracity of the results obtained using the CFD analysis, the outlet temperature of the CO_2 (T_{CO2_out}) and the average temperature where the heat flux is extracted (T_{cu}), are compared between experimental data from the refrigeration facility and the CFD results for the heat exchanger C0 (used in the experimental setup). The comparison can be seen in Fig. 7 and shows a great agreement between the experimental data and the CFD analysis with all of the results between the $\pm 5\%$ and $\pm 7\%$ interval, for the outlet temperature of the CO_2 (T_{CO2_out}) and the average temperature where the heat flux is extracted (T_{cu}), respectively.

In addition, Fig. 8 displays the temperature profile of C0 under different working pressures, 83 and 86 bar. It demonstrates how the model properly follows the rapid change in properties of the CO_2 as it gets closer to the pseudocritical pressure. At 83 bar the enhanced heat transfer properties of the CO_2 result in a closer temperature of the copper block to the fluid in comparison with the 86 bar case. Lastly, the CO_2 cools down less at 83 bar which shows how the simulations are also able to represent the effect of the increased specific heat coefficient when closer to the pseudocritical pressure.

The results obtained through the CFD analysis for the thermal resistance of the heat exchangers of the cold side (C0 and C1), show a clear tendency with the average temperature of the fluid for each pressure as it can be seen in Fig. 9. Both heat exchangers show a rapid decrease in the thermal resistance as the temperature of the fluid increases, getting closer to the pseudo-critical point for each pressure. It is also worth to

notice that in both cases, at lower pressures, the thermal resistance of the heat exchanger is lower for the same average temperature of the fluid. Finally, the thermal resistance of the optimized heat exchanger, C1, shows a clear improvement due to greater velocity of the fluid and higher inner heat exchange area.

The thermal resistance of the heat exchangers of the cold side is manually introduced in the model as a function of the average temperature of the fluid for each pressure, as in Eq. (3). Using the computational model, the effect of using different heat exchangers for the cold side of the thermoelectric subcooler is calculated. The results obtained are presented in Section 4.2.

4. Results and discussion

The data obtained with the computational model is presented and discussed in this section. Results for the different heat sinks of the hot side are shown in Section 4.1 and the results for the different heat exchangers of the cold side are shown in Section 4.2. Finally, in Section 4.3, the data obtained with the best performing hot and cold side heat exchangers is presented and discussed.

To compare the effect of the heat exchangers the evaporation level (T_0) is set to $-10\,°C$, the ambient temperature (T_{amb}) to $30\,°C$, the ambient humidity to 55%, the useful superheating (USH) to 4 K and the non-useful superheating ($NUSH$) to 12 K. The voltage supplied to the TEM (V_{TEM}) and the gas-cooler pressure (P_{gc}) are introduced in the computational model for a certain range due to their great impact on the performance of the system. The voltage supplied to the TEM goes from 1 to 4 V in 0.1 V increments and the gas-cooler pressure goes from 82 to 88 bar in 0.1 bar increments, obtaining the optimal operation point for each heat exchanger.
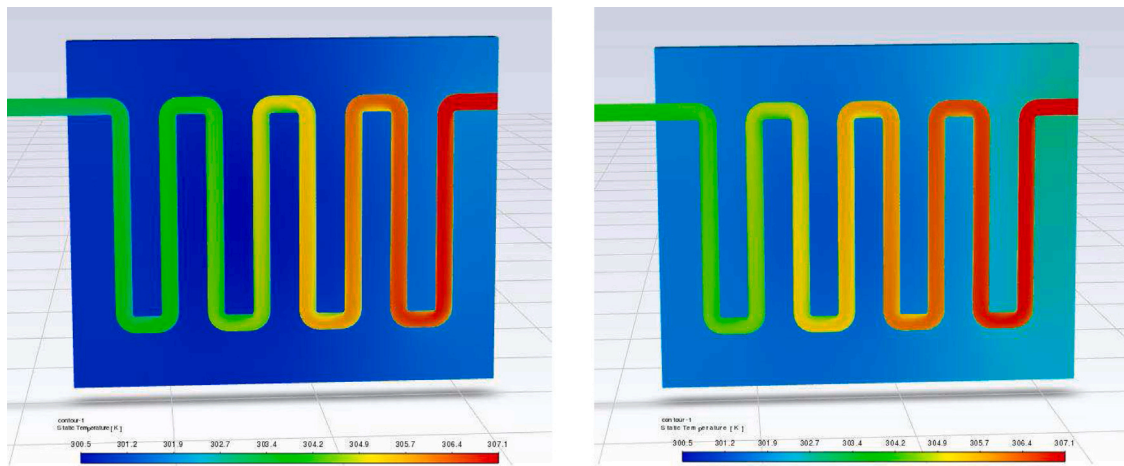
(a) Temperature profile of C0 at 86 bar

(b) Temperature profile of C0 at 83 bar

Fig. 8. Temperature profile of C0 cold side heat exchanger: (a) 80 bar and (b) 86 bar (T_{CO2_in} = 34 °C and $\dot{Q}_{HX}$ = 20 W).
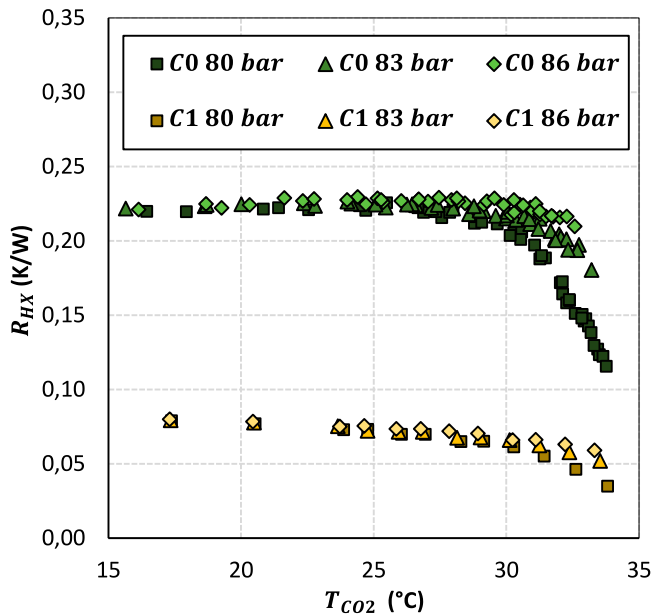

Fig. 9. Thermal characterization via CFD analysis of C0 and C1 as a function of the average temperature of the fluid for pressures 80, 83 and 86 bar.

Fig. 10. COP of the refrigeration cycle versus nominal air flow of the fans for the heat sinks H0, H1, H2 and H3.

4.1. Hot side heat sinks results

The COP of the complete refrigeration system, which is calculate as in Eq. (4), is obtained for each heat sink and fan combination under optimum working conditions (V_{TEM} and P_{gc}). The results are shown in Fig. 10, where the COP is represented versus the nominal air flow of the fans. First of all, is important to highlight that when the system is working without the fans, the COP of the facility drops drastically due to poor performance of the heat sinks. When excluding the results without the fans the COP of the refrigeration facility decreases as nominal air flow increases. This effect is related to the increase in consumption of the fans as nominal air flow increases. The improvements on the subcooler obtained with more powerful fans does not compensate the increase in consumption and results in a lower COP of the system. Worth to notice is also that F0 and F4 nominal air flow is really low which indicates that there is no need of strong forced convection for this heat sinks. Therefore, this air flow current for the hot side heat
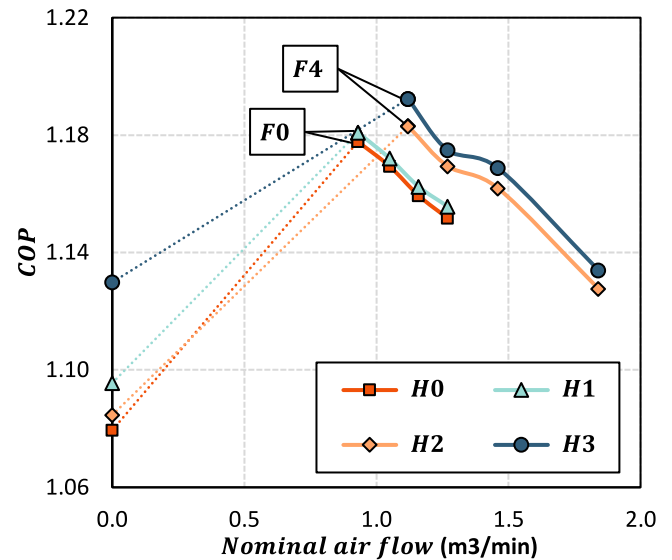
sinks could be obtained by taking advantage of the axial fan of the gas-cooler, eliminating the need of fans for the hot side heat sinks while maintaining forced convection. The best performing heat sink is H3 in combination with fan F4, the least powerful fan tested for this heat sink, with a total COP of the refrigeration cycle of 1.192.

$$COP = \frac{\dot{Q}_0}{\dot{W}_{Comp} + \dot{W}_{TESC}} = \frac{\dot{Q}_0}{\dot{W}_{Comp} + \dot{W}_{TEM} + \dot{W}_{fan}} \qquad (4)$$

As the COP of the refrigeration facility depends drastically on the working conditions of the system (V_{TEM} and P_{gc}), the effect of the heat sinks on the working conditions is analysed. The COP of the system for each heat sink of the hot side is represented versus the pressure of the gas cooler and the voltage of the TEMs in Fig. 11. The optimum working points are highlighted in the graphs and summarized in Table 8. In this table, the relative improvement in COP regarding the experimental system (H0) and the average thermal resistance on the subcooler are also included. As the thermal resistance of the heat sink on the hot side decreases from 0.36 to 0.19 K/W the optimum gas-cooler pressure is reduced from 84.6 to 84.1 bar and the optimum voltage supplied to the TEMs increases from 2.5 to 2.7 V. Regarding the COP of the system, the
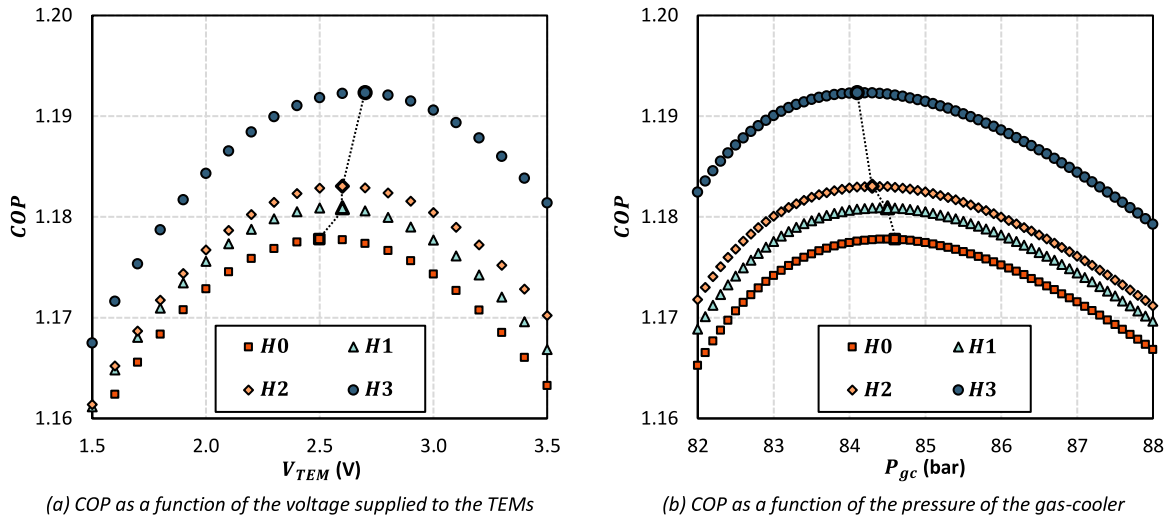
(a) COP as a function of the voltage supplied to the TEMs

(b) COP as a function of the pressure of the gas-cooler

Fig. 11. COP of the refrigeration cycle versus voltage supplied to the TEMs and gas cooler pressure for hot side heat sinks H0, H1, H2 and H3 (C0 in the cold side).

Table 8
Optimum working points for the hot side heat sinks.

Hot side HX	Fan	R_{Hot_HX} (K/W)	V_{TEM} (V)	P_{gc} (bar)	COP (/)	ΔCOP (%)
H0	F0	0.36	2.5	84.6	1.178	–
H1	F0	0.33	2.6	84.5	1.181	0.26
H2	F4	0.27	2.6	84.3	1.183	0.45
H3	F4	0.19	2.7	84.1	1.192	1.23

Table 9
Optimum working points for the cold side heat exchangers.

Cold side HX	R_{Cold_HX} (K/W)	V_{TEM} (V)	P_{gc} (bar)	COP (/)	ΔCOP (%)
C0	0.22	2.5	84.6	1.178	–
C1	0.07	2.6	84.2	1.190	1.06%

high profile heat pipe, H3, outperforms the rest of the heat sinks with an optimum COP of 1.192 at a gas-cooler pressure of 84.1 bar and a voltage supplied to the TEMs of 2.7 V. This results show the impact that the performance of the hot side heat sinks has on the COP of the whole system, exhibiting and improvement in the COP of 1.23% through an optimization of the hot side heat sinks of the thermoelectric subcooler.

4.2. Cold side heat exchangers results

The optimum working conditions for C0 and C1 are obtained and the COP of the whole system is calculated. The effect of the heat exchangers on the working conditions of the system is analysed and represented in Fig. 12. The optimum working points are highlighted in the graphs and summarized in Table 9. As the thermal resistance of the heat exchanger of the cold side decreases from 0.22 to 0.07 K/W, the optimum working pressures is reduced from 84.6 to 84.2 bar. Also, the decrease in thermal resistance rises the optimum voltage supplied to the TEMs from 2.5 to 2.6 V. Heat exchanger C1 performs better than C0, resulting in a COP of the system of 1.19 at a gas-cooler pressure of 84.2 bar and a voltage supplied to the TEMs of 2.6 V. This, represents an improvement of 1.06% in the COP of the whole system with the optimized design of the cold side heat exchanger.

4.3. Optimized subcooler results

Lastly, the system is simulated using the best performing heat exchanger for the hot and cold side (H3 and C1). The results obtained are summarized in Table 10 for: the base cycle without subcooler, the

starting setup (H0 and C0), the optimized cold side (H3 and C0), the optimized hot side (H0 and C1) and the final optimization of the whole subcooler (H3 and C1).

The percentage improvements of the cooling power and the COP ($\Delta \dot{Q}_0$ and ΔCOP) are compared to the starting setup with the TESC (H0 and C0) and are obtained as Eq. (5) shows.

$$\Delta x = \frac{x - x_{H0\ C0}}{x_{H0\ C0}} \cdot 100 \tag{5}$$

When the heat exchangers of both sides of the TESC are optimized (H3 and C1), the optimum gas-cooler pressure is reduced from 84.6 to 83.9 bar and the optimal voltage supplied to the TEMs increases from 2.5 to 2.7 V. Also, the subcooling produced notably rises, going from 8.2 to 10.4. Through the optimization of the heat exchangers of the subcooler, a final improvement on the COP of 2.49% is obtained for the whole refrigeration system. It is also worth to notice that the cooling capacity ($\dot{Q}_0$) increases after the optimization, from 356 to 370.3 W, resulting in a 4% increment in the cooling power of the system. This result exhibits the importance of the optimization of the heat exchangers and their impact in the performance of the transcritical CO_2 cycle with thermoelectric subcooler, in terms of COP and cooling capacity.

The decrease of the thermal resistances of the heat exchangers improves the heat transfer at both sides of the TEM. This produces a lower thermal gradient at the TEM which improves the efficiency of the modules. With the new reduced thermal resistances, the system benefits from working at higher supplied voltages to the TEMs. This finally results in an increased subcooling degree in the refrigeration system that improves the cooling capacity. In addition, as vapour compression systems with greater subcooling degrees benefit from working at lower working pressures, the optimum working pressure of the cycle decreases which further improves the COP of the refrigeration system.

Regarding the hot side heat exchanger, it has been demonstrated that with a low air flow current the heat exchangers performs properly. This low air flow could be obtained by taking advantage of the greater axial fan of the gas-cooler, removing the extra consumption of the fans of the subcooler and improving the COP of the system. In the optimized case, if the power consumption of the fans was not taken into account the COP of the system would rise from 1.207 to 1.236 and the improvement from the starting setup would augment to almost 5%. This data displays the importance on the design of the thermoelectric subcooler in conjunction with the base transcritical CO_2 refrigeration cycle and the improvements that an ingenious design can have on the performance of the combined system.

(a) COP as a function of the voltage supplied to the TEMs

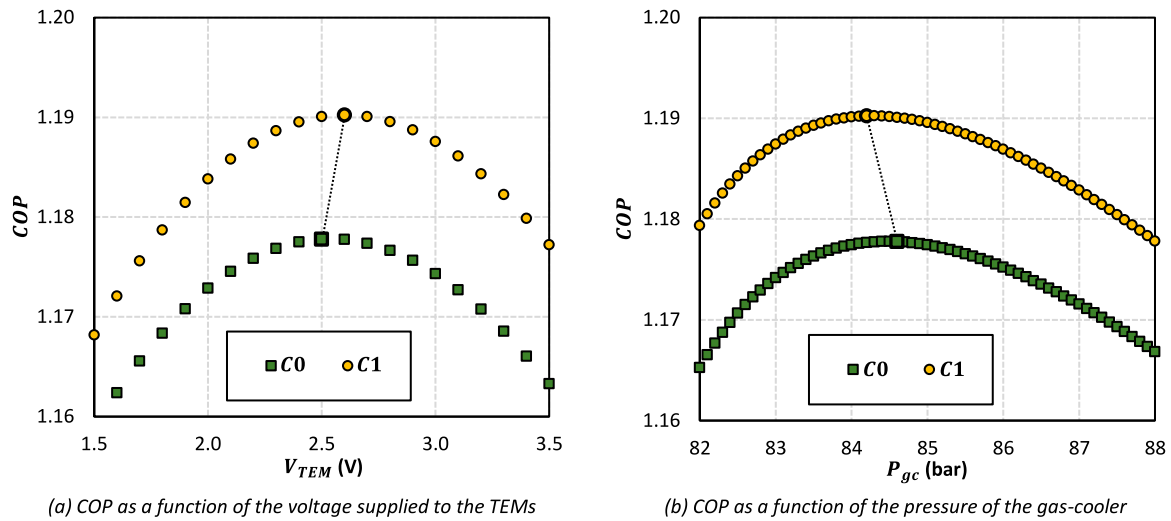(b) COP as a function of the pressure of the gas-cooler

Fig. 12. COP of the refrigeration cycle versus voltage supplied to the TEMs and gas cooler pressure for cold side heat exchangers C0 and C1 (H0 on the hot side).

Table 10
Summary of the calculated results for optimum working conditions.

		R_{Hot_HX} (K/W)	R_{Cold_HX} (K/W)	V_{TEM} (V)	Sub (K)	P_{gc} (bar)	$\dot{Q}_0$ (W)	COP (/)	$\Delta \dot{Q}_0$ (%)	ΔCOP (%)	$\Delta \dot{Q}_{0\,Base}$ (%)	ΔCOP_{Base} (%)
Base cycle	No TESC	–	–	–	–	86.7	293.2	1.052	–	–	–	–
Starting setup	H0 & C0	0.36	0.22	2.5	8.2	84.6	356.0	1.178	–	–	21.4	11.96
Hot side optimization	H3 & C0	0.19	0.22	2.7	9.7	84.1	365.8	1.192	2.7	1.23	24.8	13.34
Cold side optimization	H0 & C1	0.36	0.07	2.6	9.1	84.2	361.7	1.190	1.6	1.06	23.4	13.14
Optimized subcooler	H3 & C1	0.19	0.07	2.7	10.4	83.9	370.3	1.207	4.0	2.49	26.3	14.75

The calculated results are also compared with the base transcritical CO_2 cycle without the thermoelectric subcooler, to further understand the effects of the optimization of the heat exchangers of the subcooler. The percentage improvements of the cooling power and the COP ($\Delta \dot{Q}_{0\,Base}$ and ΔCOP_{Base}) are compared to the base transcritical carbon dioxide cycle without the subcooler as in Eq. (6).

$$\Delta x_{Base} = \frac{x - x_{Base}}{x_{Base}} \cdot 100 \qquad (6)$$

The base cycle shows a COP of 1.052 with a cooling capacity of 293.2 W at a gas-cooler pressure of 86.7 bar. With the starting setup of the thermoelectric subcooler, the refrigeration cycle presents a COP of 1.178 with a cooling capacity of 356 W. In terms of percentage improvements, the starting setup of the subcooler presents an upgrade in the COP and the cooling capacity of 11.96% and 21.4%, respectively. When the thermoelectric subcooler is optimized, the percentage improvements rises to 14.75% for the COP and to 26.3% for the cooling capacity of the system. These numbers exhibit the importance of proper optimization of the heat exchangers on a thermoelectric subcooler to boost the performance of the complete refrigeration cycle.

5. Conclusions

This work evaluates the impact that the heat exchangers of a thermoelectric subcooler, included in a transcritical CO_2 refrigeration cycle, have, on the performance of the whole cooling facility. An advanced computational model has been used to calculate, in terms of coefficient of performance, cooling capacity and optimum working parameters, the effect of using different heat exchangers in both the hot and cold side of the thermoelectric subcooler.

For the hot side, 4 different commercial heat sinks have been experimentally characterized and introduced in the computational model. Regarding the cold side, 2 heat sinks have been characterized using Computational Fluid Dynamics Software Ansys Fluent and implemented in the computational model.

Through the optimization of the heat exchangers of the thermoelectric subcooler, the thermal resistance of the hot side heat sink is reduced from 0.36 to 0.19 K/W, and the thermal resistance of the cold side heat exchanger decreases from 0.22 to 0.07 K/W with, the following results in the system:

1. The optimum working pressure drops from 84.6 to 83.9 bar.
2. The optimum voltage supplied to the thermoelectric modules rises from 2.5 to 2.7 V.
3. The coefficient of performance of the refrigeration cycle increases from 1.178 to 1.207 with a percentage increment of 2.49%.
4. The cooling capacity of the system increases up to 4%, from 356 to 370.3 W.

The starting setup of the subcooler showed an upgrade in the coefficient of performance of 11.96% and an increase in cooling capacity of 21.4%. Through the optimization of the heat exchangers of the thermoelectric subcooler, the improvements in the coefficient of performance and cooling capacity are boosted to 14.75% and 26.3%, respectively. These results exhibit the importance of proper optimization, design and operation of a thermoelectric subcooler and the impact that the heat exchangers have in the performance of the whole refrigeration facility.

Declaration of competing interest

The authors declare that they have no known competing financial interests or personal relationships that could have appeared to influence the work reported in this paper.

Acknowledgements

References

[1] I.E. Agency, Electricity market report - jan 2022, 2022.

[2] I.E. Agency, Electricity market report - jul 2021, 2021, URL www.iea.org/t&c/.

[3] IIR, 38th informatory note on refrigeration technologies / The role of refrigeration in the global economy, 2019.

[4] L. Nebot-Andrés, J. Catalán-Gil, D. Sánchez, D. Calleja-Anta, R. Cabello, R. Llopis, Experimental determination of the optimum working conditions of a transcritical CO2 refrigeration plant with integrated mechanical subcooling, Int. J. Refrig. 113 (2020) 266–275, http://dx.doi.org/10.1016/j.ijrefrig.2020.02.012.

[5] D. Sánchez, J. Patiño, R. Llopis, R. Cabello, E. Torrella, F.V. Fuentes, New positions for an internal heat exchanger in a CO2 supercritical refrigeration plant. Experimental analysis and energetic evaluation, Appl. Therm. Eng. 63 (2014) 129–139, http://dx.doi.org/10.1016/j.applthermaleng.2013.10.061.

[6] J. Sarkar, N. Agrawal, Performance optimization of transcritical CO2 cycle with parallel compression economization, Int. J. Therm. Sci. 49 (2010) 838–843, http://dx.doi.org/10.1016/j.ijthermalsci.2009.12.001.

[7] J. Catalán-Gil, L. Nebot-Andrés, D. Sánchez, R. Llopis, R. Cabello, D. Calleja-Anta, Improvements in CO2 booster architectures with different economizer arrangements, Energies 13 (2020) http://dx.doi.org/10.3390/en13051271.

[8] D. Li, E.A. Groll, Transcritical CO2 refrigeration cycle with ejector-expansion device, Int. J. Refrig. 28 (2005) 766–773, http://dx.doi.org/10.1016/j.ijrefrig.2004.10.008.

[9] B. Zhang, D. Zhao, Y. Zhao, H. Ji, L. Chen, L. Liu, Comparative analysis of typical improvement methods in transcritical carbon dioxide refrigeration cycle, Procedia Eng. 205 (2017) 1207–1214, http://dx.doi.org/10.1016/j.proeng.2017.10.355.

[10] P. Aranguren, D. Sánchez, A. Casi, R. Cabello, D. Astrain, Experimental assessment of a thermoelectric subcooler included in a transcritical CO2 refrigeration plant, Appl. Therm. Eng. 190 (2021) http://dx.doi.org/10.1016/j.applthermaleng.2021.116826.

[11] C. Wu, S. sen Wang, X. jia Feng, J. Li, Energy, exergy and exergoeconomic analyses of a combined supercritical CO 2 recompression brayton/absorption refrigeration cycle, 2017, http://dx.doi.org/10.1016/j.enconman.2017.05.042.

[12] R. Radermacher, B. Yang, Innovative thermoelectric-assisted vapor-compression refrigeration systems, 2005.

[13] J. Schoenfeld, J. Muehlbauer, Y. Hwang, R. Radermacher, orderlithtml Schoenfeld, Integration of a thermoelectric subcooler into a carbon dioxide transcritical vapor compression cycle refrigeration system, 2008, URL http://docs.lib.purdue.edu/iracc/903.

[14] J. Sarkar, Performance optimization of transcritical CO2 refrigeration cycle with thermoelectric subcooler, Int. J. Energy Res. 37 (2013) 121–128, http://dx.doi.org/10.1002/er.1879.

[15] K. Yazawa, S. Dharkar, O. Kurtulus, E.A. Groll, Optimum Design for Thermoelectric in a Sub-cooled Trans-critical CO2 Heat Pump for Data Center Cooling, IEEE, 2015.

[16] S. Jamali, M. Yari, F. Mohammadkhani, Performance improvement of a transcritical CO2 refrigeration cycle using two-stage thermoelectric modules in sub-cooler and gas cooler, Int. J. Refrig. 74 (2017) 105–115, http://dx.doi.org/10.1016/j.ijrefrig.2016.10.007.

[17] D. Sánchez, P. Aranguren, A. Casi, R. Llopis, R. Cabello, D. Astrain, Experimental enhancement of a CO2 transcritical refrigerating plant including thermoelectric subcooling, Int. J. Refrig. 120 (2020) 178–187, http://dx.doi.org/10.1016/j.ijrefrig.2020.08.031.

[18] L. Catalan, P. Aranguren, M. Araiz, G. Perez, D. Astrain, New opportunities for electricity generation in shallow hot dry rock fields: A study of thermoelectric generators with different heat exchangers, Energy Convers. Manage. 200 (2019) http://dx.doi.org/10.1016/j.enconman.2019.112061.

[19] D. Astrain, P. Aranguren, A. Martínez, A. Rodríguez, M.G. Pérez, A comparative study of different heat exchange systems in a thermoelectric refrigerator and their influence on the efficiency, Appl. Therm. Eng. 103 (2016) 1289–1298, http://dx.doi.org/10.1016/j.applthermaleng.2016.04.132.

[20] M.A. Moradkhani, S.H. Hosseini, M. Mansouri, G. Ahmadi, M. Song, Robust and universal predictive models for frictional pressure drop during two-phase flow in smooth helically coiled tube heat exchangers, Sci. Rep. 11 (2021) http://dx.doi.org/10.1038/s41598-021-99476-6.